Remote sensing of aerosols over land surfaces from POLDER-ADEOS-1 polarized measurements

J. Deuzé, F.M. Bréon, C. Devaux, P. Goloub, M. Herman, B. Lafrance, F. Maignan, A. Marchand, F. Nadal, G. Perry, et al.

JOURNAL OF GEOPHYSICAL RESEARCH, VOL. 106, NO. D5, PAGES 4913–4926, MARCH 16, 2001

Remote sensing of aerosols over land surfaces from POLDER-ADEOS–1 polarized measurements

J. L. Deuzé,[1] F. M. Bréon,[2] C. Devaux,[1] P. Goloub,[1] M. Herman,[1] B. Lafrance,[3] F. Maignan,[2] A. Marchand,[1] F. Nadal,[2] G. Perry,[1] and D. Tanré[1]

Abstract. The polarization measurements achieved by the POLDER instrument on ADEOS-1 are used for the remote sensing of aerosols over land surfaces. The key advantage of using polarized observations is their ability to systematically correct for the ground contribution, whereas the classical approach using natural light fails. The estimation of land surface polarizing properties from POLDER has been examined in a previous paper. Here we consider how the optical thickness δ_0 and Ångström exponent α of aerosols are derived from the polarized light backscattered by the particles. The inversion scheme is detailed, and illustrative results are presented. Maps of the retrieved optical thickness allow for detection of large aerosol features, and in the case of small aerosols, the δ_0 and α retrievals are consistent with correlative ground-based measurements. However, because polarized light stems mainly from small particles, the results are biased for aerosol distributions containing coarser modes of particles. To overcome this limitation, an aerosol index defined as the product $AI = \delta_0\alpha$ is proposed. Theoretical analysis and comparison with ground-based measurements suggest that AI is approximately the same when using δ_0, and α is related to the entire aerosol size distribution or derived from the polarized light originating from the small polarizing particles alone. This invariance is specially assessed by testing the continuity of AI across coastlines, given the unbiased properties of aerosol retrieval over ocean. Although reducing the information concerning the aerosols, this single parameter allows a link between the POLDER aerosol surveys over land and ocean. POLDER aerosol index global maps enable the monitoring of major aerosol sources over continental areas.

1. Introduction

Recognition of the climatic influence of aerosols [*Hansen and Lacis*, 1990; *Charlson et al.*, 1992] has led to large efforts for improving their global monitoring by satellite. Over the ocean, where the aerosol remote sensing is tractable from measurements at near-infrared wavelengths, aerosol surveys using satellite imagery have been conducted from decades [*Fraser*, 1976; *Quentzel and Koepke*, 1984; *Rao et al.*, 1989; *Nakajima and Higurashi*, 1998]. Presently, aerosol maps are derived routinely from NOAA/AVHRR data [*Stowe et al.*, 1992; *Husar et al.*, 1997], and improved characterization of the aerosols is or should be derived from new remote sensing instruments like OCTS (Ocean Color Temperature Scanner) [*Nakajima et al.*, 1999]. SeaWiFS (Sea-viewing Wide Field-of-view Sensor) [*Gordon and Wang*, 1994], POLDER (Polarization and Directionality of Earth's Reflectances) [*Deuzé et al.*, 1999], MISR (Multiangle Imaging Spectroradiometer) [*Kahn et al.*, 1998], or MODIS (Moderate-Resolution Imaging Spectroradiometer) [*Tanré et al.*, 1997].

By contrast, the aerosol remote sensing over land surfaces, where the main aerosol sources are located, is much less advanced because of the difficulty in discriminating the aerosol contribution from the ground in top of the atmosphere (TOA) measurements. This problem has been approached in several different ways, for example, from the reflectance of dark targets [*Kaufman and Sendra*, 1988], the adjacency effect of the aerosols [*Kaufman and Joseph*, 1982; *Tanré et al.*, 1988], or their effect on the apparent temperature of desertic areas [*Legrand et al.*, 1988]. Recently, first monitoring of UV-absorbing aerosols, both over land and ocean, has been achieved by using the ultraviolet measurements of TOMS/Nimbus 7 [*Herman et al.*, 1997; *Torres et al.*, 1998]. Here again, the new generation of remote sensing instruments should improve the characterization of the aerosols from dark dense vegetation reflectance [*Kaufman et al.*, 1997a, 1997b], multiangle imagery [*Martonchik*, 1997] or polarization measurements [*Herman et al.*, 1997]. Here we examine the capacity of directional polarization measurements, using the 8 month data acquired by POLDER aboard ADEOS-1. The remote sensing of aerosols is based on the polarized light that they backscatter and the expectation that any correction in TOA measurements of the polarized light reflected by surfaces should be more tractable than the correction of the total reflected light.

The wide field-of-view imaging spectroradiometer POLDER, on ADEOS-1 from November 1996 to the end of ADEOS on June 1997, offered multispectral, multidirectional, and polarized measurements of the Earth's reflectances. The wide field-of-view optics and the matrix array detector of POLDER provide bidimensional pictures of the Earth's surface which allow daily observations with a resolution of 6 km ×

[1]Laboratoire d'Optique Atmosphérique, Université de Lille, Villeneuve d'Ascq, France.
[2]Laboratoire des Sciences du Climat et de l'Environnement, Gif sur Yvette, France.
[3]Centre National d'Etudes Spatiales, Toulouse, France.

Paper number 2000JD900364.
0148-0227/01/2000JD900364$09.00

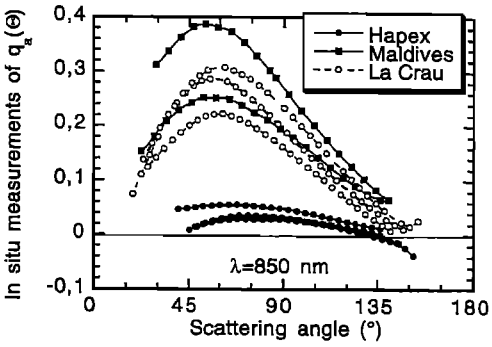

Figure 1. In situ measurements of the polarized phase functions $q_a(\Theta)$ for different kinds of aerosols as a function of the scattering angle Θ; $q_a(\Theta)$ is derived from ground-based measurements of the polarized skylight at wavelength $\lambda = 865$ nm [*Vermeulen et al.*, 2000]. Results are shown for desertic dusts (Hapex campaign, Maldives), aerosols from the Indian continent (Indoex campaign), and urban-industrial aerosols (La Crau campaign).

7 km, from 13 different viewing geometries during the same orbit. A rotating filter wheel provides radiance measurements in nine channels ranging from 443 to 910 nm. Moreover, the channels centered at 443, 670, and 865 nm are equipped with polaroids, therefore permitting measurements of the polarization [*Deschamps et al.*, 1994].

The aerosol retrieval from these measurements is detailed in section 2. The polarized light scattered by the aerosols is firstly estimated by correcting the molecular and surface influences, which requires modeling of the POLDER measurements and surface bidirectional polarization distribution function (BPDF). By processing multitemporal series of POLDER data, *Nadal and Bréon* [1999] have developed BPDF models of the land surfaces which have been entered in the inversion scheme in order to derive the aerosol contribution. Presently, the 443 nm data are not used. At this wavelength the molecular contribution dominates largely the measurements, so because of the uncertainty in the calibration factor of the blue channel, there is very little accuracy in the remaining aerosol contribution to use in an aerosol inversion scheme. Finally, comparison of the aerosol polarization measurements in the 670 and 865 nm channels along with calculations for a set of aerosol models provides the optical thickness of the particles δ_0 at $\lambda_0 = 865$ nm and their Ångström exponent α between wavelengths $\lambda_0 = 865$ nm and $\lambda_1 = 670$ nm such that $\delta_1 = \delta_0(\lambda_1/\lambda_0)^{-\alpha}$, where δ_1 is the optical thickness at λ_1.

The applicability of the method is examined in section 3, and examples of level 2 aerosol products, α and δ_0, over land are shown. Some large aerosol features are recognizable in daily maps of the retrieved optical thickness. Section 4 presents comparisons of the POLDER results with correlative ground-based measurements. The retrieved parameters α and δ_0 are significant in the case of small aerosols, such as in biomass burning events, but are generally biased. Because polarized light is mainly sensitive to scattering by small particles and cannot detect coarser modes of aerosols, α and δ_0 are probably related to the smaller mode of particles, leading to an overestimation of the Ångström exponent and an underestimation of the optical thickness in the case of bimodal size distribution of the particles. In a first approach it is proposed, in section 5, to combine the parameters α and δ_0 into a simple aerosol index, $AI = \alpha\delta_0$, which should be approximately the same when calculated either with the biased parameters derived from polarization or with those corresponding to the whole size distribution. This aerosol index makes it possible to link the two different aerosol surveys performed by POLDER over land and over the ocean, and global maps of AI provide a new monitoring opportunity of major aerosol sources over continental areas, including desertic particles.

2. Aerosol Retrieval From Polarized Light

2.1. Scheme of Aerosol Retrieval

The principle of the method has been discussed previously [*Herman et al.*, 1997]. Ground-based measurements suggest that the polarized light reflected by ground targets is small and stable enough to allow for correction in TOA measurements, and we assume that these surface BPDFs have been determined. Then, the POLDER data can provide the polarized light scattered by the aerosols at several wavelengths λ, and for several scattering angles Θ, this is about $\delta_a q_a(\Theta)$, where δ_a is the optical thickness of the aerosols and $q_a(\Theta)$ is their polarized phase function; that is,

$$q_a(\Theta) = p_a(\Theta)P_a(\Theta), \quad (1)$$

where $p_a(\Theta)$ is the phase function and $P_a(\Theta)$ is the polarization ratio for single scattering of the aerosols. The derivation of $\delta_a q_a(\Theta)$ from the measurements is detailed in section 2.2. We examine here how the aerosol retrieval may be achieved from $\delta_a q_a(\Theta)$, instead of $\delta_a p_a(\Theta)$, used in the classical approach of total radiance measurements.

The inversion seems more delicate because the polarized phase function $q_a(\Theta)$ is more versatile than the normalized phase function $p_a(\Theta)$. Ground-based measurements, however, suggest that at near-infrared wavelengths ($\lambda = 850$ nm to $\lambda = 1650$ nm), $q_a(\Theta)$ is reasonably defined for many terrestrial aerosols [*Vermeulen et al.*, 2000]. Figure 1 shows examples of $q_a(\Theta)$ functions measured from the ground for different kinds of aerosols. Most aerosols exhibit rather stable polarized phase functions, except desertic particles whose polarization is typically 5–10 times lower. POLDER measurements now taken over the ocean will enable estimations of $q_a(\Theta)$ for a broader class of terrestrial aerosols. The present scheme is based on monomodal aerosol models whose polarization exhibits similar behavior to that of the data set in Figure 1. Lognormal size distributions have been retained (see section 2.3), with a fixed value for the standard deviation σ, and several values of the modal radius $\bar{r}$, and refractive index m, of the aerosols. Figure 2 shows examples of the resulting polarized phase functions, for $m = 1.40$. They are in reasonable agreement with the observations.

To select the best model from the measurements, one may look at the directional behavior of $q_a(\Theta)$ within the different viewing directions of POLDER, or/and to the spectral behavior of $\delta_a q_a(\Theta)$ in the three polarized channels. The interval of scattering angles varies from a few degrees to more than 80° depending on the target latitude and localization within the POLDER swath [*Bréon et al.*, 1997]. As explained previously, the present results are obtained by using only the 670 and 865 nm data. In these conditions, Figures 3 and 4 show that retrieval of the aerosol model is rather delicate.

For a few models, Figure 3 shows how $q_a(\Theta)/q_a(100°)$ varies according to the particle refractive index and Ångström

exponent (or particle mean dimension) at $\lambda_0 = 865$ nm. Except for large particles, which exhibit characteristic polarization features in backscattering directions, the expected directional effects are quite small. Practically, for α larger than 1.35, the $q_a(\Theta)$ functions in Figure 3 differ only by a multiplicative factor.

On the other hand, for the same aerosol models, Figure 4 shows how the polarized light varies as a function of the observation wavelength. The spectral dependance of the polarized light is estimated here by

$$X(\lambda) = \delta_a(\lambda)q_a(\lambda, \Theta_0)/\delta_a(\lambda_0)q_a(\lambda_0, \Theta_0), \qquad (2)$$

with $\Theta_0 = 100°$ and $\lambda_0 = 850$ nm. The spectral information is much more reliable than the directional one, although restricting to channels at 670 and 865 nm limits the sensitivity of the method.

2.2. Modeling of the Measurements

We consider cloud-free POLDER pixels, selected according to the cloud-screening algorithm of *Bréon and Colzy* [1999]. Preliminary correction of the influences of the gaseous absorption [*Hagolle et al.*, 1999; *Vesperini et al.*, 1999] and of the stratospheric aerosol contribution [*Lafrance and Herman*, 1998] is performed. To reduce the noise level, the aerosol algorithm is applied to 3 × 3 POLDER pixels (i.e., about 20 km × 20 km areas). Moreover, viewing directions corresponding to specular reflection within 3° are eliminated in order to avoid contamination by the Sun glint from subpixel water surfaces (e.g., lakes, bogs).

The partially polarized light at TOA is assumed to be linearly polarized, and the three measurements performed in a POLDER-polarized channel are converted [*Hagolle et al.*, 1996] into the Stokes parameters (I_0, Q_0, U_0) with

$$I_0 = L, \qquad Q_0 = L_p \cos(2\psi_0), \qquad U_0 = L_p \sin(2\psi_0), \qquad (3)$$

where L and L_p are the normalized radiance and polarized radiance; that is, $L(L_p) = \pi L^*(L_p^*)/E$ where E is the solar irradiance at TOA and $L^*(L_p^*)$ is the radiance (polarized radiance). Here the Stokes parameters are referred to axes linked to the meridian plane, which contains the viewing direction; hence in (3), ψ_0 is the angle between the polarization direction and the meridian plane $(-\pi/2 < \psi_0 < +\pi/2)$. The accuracy of the polarization measurements has been controlled by using observations of the Sun glint over the ocean [*Toubbé et al.*, 1999] and is estimated at approximately ±2% polarization [*Hagolle et al.*, 1999].

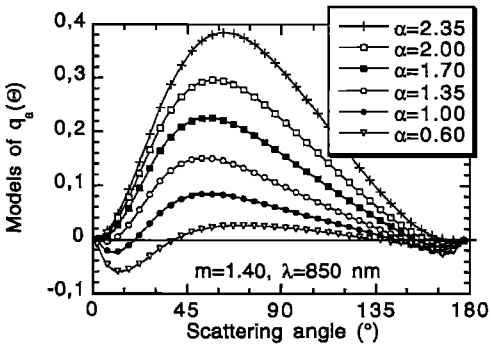

Figure 2. Examples of the polarized phase functions $q_a(\Theta)$ at $\lambda = 865$ nm for the monomodal models used in the inversion scheme, according to the corresponding modal radius $\bar{r}$ or the corresponding Ångström exponent α. The assumed refractive index of the particles is $m = 1.40$.

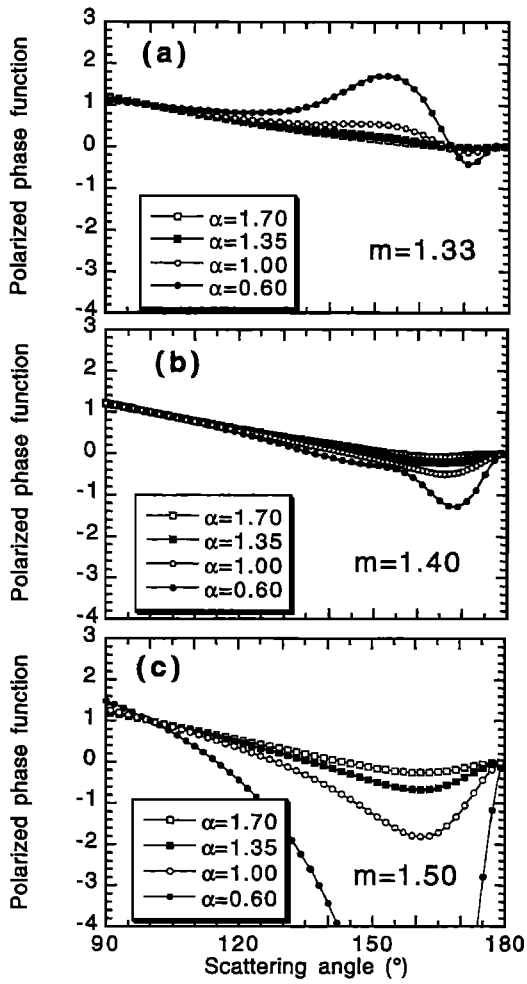

Figure 3. (a) Directional dependence of the polarized light. Behavior of $q_a(\Theta)/q_a(100°)$ as a function of Θ for monomodal models with refractive index $m = 1.33$. Large particles exhibit characteristic polarization features but for small particles ($\alpha > 1.35$) no information on $\bar{r}$ and m (see Figures 3b and 3c), hence on $q_a(\Theta)$, can be derived from the angular dependence of polarized light. (b) Same as Figure 3a but for particle refractive index $m = 1.40$. (c) Same as Figure 3a but for particle refractive index $m = 1.50$.

Given the uncertainties, the measurements are modeled in a simplified way by considering only the polarized light corresponding to single scattering by aerosols, single scattering by molecules, and direct reflection on the surface. Because primary scattering largely dominates the polarized light, this approximation is sufficient to take into account most of the polarized light in channels centered at 670 and 865 nm, where molecular scattering is small, and for aerosol optical thickness smaller than about 0.25 [*Bréon et al.*, 1997; *Lafrance*, 1997]. Single scattering by molecules or disordered particles gives polarized light perpendicular or parallel to the scattering plane, which contains the solar and viewing directions. Similarly, BPDFs are modeled by assuming that the polarized light comes from specular reflection on surface elements, whose normal bisects the solar and viewing directions. The resulting polarization therefore is perpendicular to the scattering plane

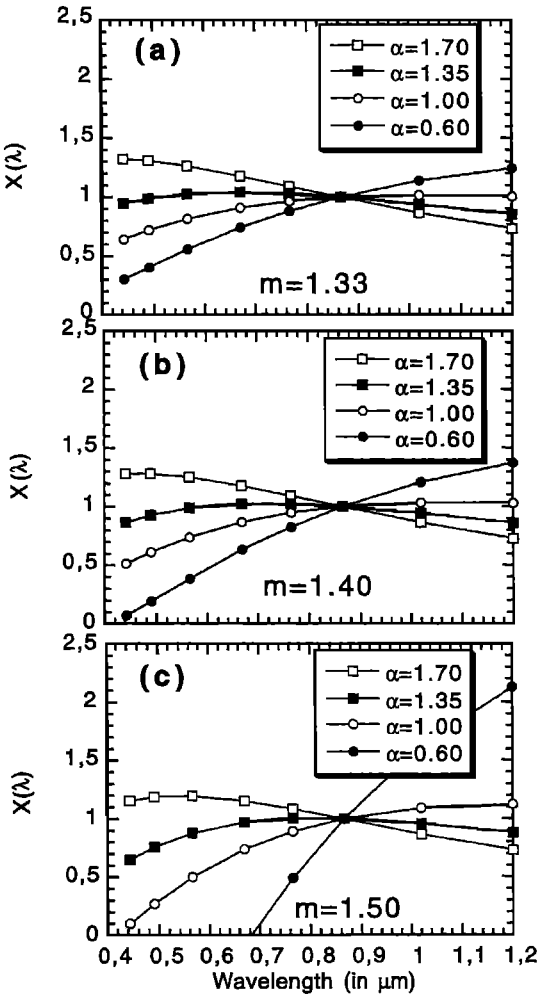

Figure 4. (a) Spectral dependence of the polarized light. Behavior of $(\delta_a q_a)_\lambda/(\delta_a q_a)_{\lambda_0}$ as a function of λ for the monomodal models of Figure 3a. The scattering angle is fixed (Θ = 100°) and λ_0 = 850 nm. The spectral behavior of polarized light is linked mainly to the behavior of $\delta_{a,\lambda}/\delta_{a,\lambda_0}$ and allows the retrieval of the particle dimension or Ångström exponent. (b) Same as Figure 4a but for particle refractive index m = 1.40. (c) Same as Figure 4a but for particle refractive index m = 1.50.

also. Thus by considering the Stokes parameters with reference to axes perpendicular and parallel to the scattering plane (i.e., with $\psi = 0$ or $\pi/2$ for the angle between the polarization direction and the normal to the scattering plane), each polarized term reduces into its Q parameter, $Q = L_p \cos(2\psi) = \pm L_p$, with

$$Q_a = \delta_a q_a(\Theta)/(4 \cos \theta_v), \tag{4a}$$

$$Q_m = \delta_m(z) q_m(\Theta)/(4 \cos \theta_v), \tag{4b}$$

$$Q_g = L_p^g(\Omega), \tag{4c}$$

where $\theta_v(\theta_s)$ is the zenith viewing (solar) angle, and Ω is the Sun incident angle on the surface element (i.e., $(\pi - \Theta)/2$); the molecular polarized phase function $q_m(\Theta)$ is positive, while the aerosol-polarized phase function $q_a(\Theta)$ may be positive or negative for polarization direction, respectively, perpendicular or parallel to the scattering plane; the BPDF modeling gives L_p^g positive; note that the molecular optical thickness $\delta_m(z)$ is scaled according to the altitude of the target. Finally, the polarized radiance at TOA, referred to this way, is written as

$$Q_{\text{cal}} = Q_m + e^{-M\delta_m}(Q_a + e^{-M\beta\delta_a} Q_g), \tag{5}$$

where M is the air mass factor, and the exponential transmission terms account for the screening effects of the upper molecular layer and aerosol layer on the polarized light from lower layers; β accounts for the large forward scattering of the aerosols, a property that reduces their screening effect on the polarized light from the ground [*Bréon et al.*, 1995; *Lafrance*, 1997]. For typical surface BPDFs and aerosol models, simulations of the TOA-polarized radiance have been performed with vertical mixing of the molecules and aerosols. The aerosol and molecular densities were given exponential profiles with scale heights of 2 and 8 km, respectively. The results show that with $\beta \approx 0.50$, (5) is accurate within about 0.0001 at 865 nm and 0.0002 at 670 nm for aerosol optical thickness smaller than 0.25 and viewing angles smaller than 60° [*Lafrance*, 1997]. The accuracy of (5) decreases for larger aerosol optical thicknesses.

On the other hand, given (Q_0, U_0) and the observation geometry, the angle ψ_{meas} between the observed polarization direction and the normal to the scattering plane is evaluated. Of course, because of the multiple scattering, scattering/reflection processes, and measurement errors, ψ_{meas} is not exactly zero or $\pi/2$. Numerical simulations, however, show that for the 865 and 670 nm wavelengths, ψ_{meas} should depart significantly from zero or $\pi/2$ only when the polarized light is nearly null. To be consistent with the simplified modeling, given $L_p^{\text{meas}} = \sqrt{Q_0^2 + U_0^2}$ and ψ_{meas}, the measured Stokes parameters with reference to the scattering plane are approximated into the form

$$Q_{\text{meas}} = \varepsilon_{\text{meas}} \sqrt{Q_0^2 + U_0^2} \quad \begin{matrix} \varepsilon_{\text{meas}} = +1 \text{ for } |\psi_{\text{meas}}| < 45° \\ \varepsilon_{\text{meas}} = -1 \text{ for } |\psi_{\text{meas}}| > 45°. \end{matrix} \tag{6}$$

Finally, given L_p^g and the known molecular term, the aerosol parameters are derived from

$$Q_{\text{meas}} = \frac{\delta_m q_m}{4 \cos \theta_v} + e^{-M\delta_m}\left(\frac{\delta_a q_a}{4 \cos \theta_v} + e^{-M\beta\delta_a} L_p^g\right). \tag{7}$$

2.3. Aerosol Inversion

Crude modelings only of surface BPDFs were known before the POLDER launch [*Vanderbilt et al.*, 1990; *Rondeaux and Herman*, 1991; *Bréon et al.*, 1995]. From a preliminary analysis of time series measurements of the polarized radiance in the 865 nm POLDER channel, *Nadal and Bréon* [1999] have developed improved BPDF models with L_p^g in the form

$$L_p^g = \alpha_0 \cos \theta_s \{1 - \exp[\beta_0 R_p(\Omega)/(\cos \theta_s + \cos \theta_v)]\}, \tag{8}$$

where $R_p(\Omega)$ is the Fresnel reflection coefficient for polarized light, calculated for a refractive index of m = 1.50; α_0 and β_0 are empirical coefficients adjusted for the different classes of land surface according to the main International Geosphere-Biosphere Programme (IGBP) biotypes and the normalized difference vegetation index (NDVI) [*Nadal and Bréon*, 1999]. Equation (8) gives values of L_p^g similar to those of the expected polarized radiance scattered by the aerosols, which explains why remote sensing of aerosols in polarized light should be feasible. We assume that the polarized light reflected by surfaces is independent on the wavelength [*Vanderbilt et al.*, 1990; *Rondeaux and Herman*, 1991; *Bréon et al.*, 1995], and so the same BPDF is used in the 670 nm channel.

The aerosol modeling consists of tabulations of the $q_a(\lambda, \Theta)$ functions and scattering coefficient $s_a(\lambda)$ of the aerosols at 670 and 865 nm. We consider spherical nonabsorbing particles with monomodal size distributions in the form

$$\frac{dN(r)}{d \ln r} = \frac{1}{\sigma\sqrt{2\pi}} \exp\left[-\frac{1}{2}\left(\frac{\ln r - \ln \bar{r}}{\sigma}\right)^2\right]. \quad (9)$$

Following *Shettle and Fenn* [1979], a value of 0.864 is used for σ. Three values of the aerosol real refractive index are considered, $m = 1.33$, 1.40, and 1.50, because of possible different behaviors of $q_a(\Theta)$ in backscattering directions depending on m (see Figure 3). For each value of m, 12 values of $\bar{r}$ are adjusted to provide Ångström exponents ranging from 0.30 to 2.50.

Given the $2N$ (two wavelengths, N-viewing directions) measurements, for each aerosol model the error η,

$$\eta = \sqrt{\frac{1}{2N} \sum_{\lambda_0,\lambda_1} \sum_j [Q_{\text{cal}}(\lambda, \Theta_j) - Q_{\text{meas}}(\lambda, \Theta_j)]^2}, \quad (10)$$

is minimized by adjusting δ_0. The retrieved aerosol parameters are the Ångström exponent α and optical thickness δ_0 corresponding to the model which gives the smallest residual error η. Examination of the measurements shows that we never observe the large polarization features corresponding to the rainbow of large particles, in Figures 2 and 3, which could provide valuable information on the particle refractive index. Therefore the refractive index corresponding to the selected model is not expected to be significant and will not be examined.

3. Results

3.1. Preliminary Qualitative Results

The ability to control the land surface contribution from satellite is a key point of the method. A qualitative illustration of this problem is shown in Plate 1. For each ground pixel of a large geographic area, pictures A and B display the maximum and minimum values of the polarized radiance measured in the 865 nm channel times cos θ_v, in the viewing direction corresponding to a constant scattering angle, $\Theta = 120°$, over a 30 day period. The measurements are corrected from the molecular term according to (4b). By selecting a constant Θ, thus a constant Ω, variations of the surface BPDF should be minimized. The 120° scattering angle provides a good repetition of the measurements at the considered latitudes and is far enough from the cloud rainbow direction (about 140°) [*Goloub et al.*, 1994] to prevent contamination of the polarized light by residual liquid clouds.

The noiseless behaviors of the pictures give confidence in the results, and the mean levels are consistent with the expected orders of magnitude. In picture A, with $\delta_a \cong 4 \cos \theta_v L_p / q_a(120°)$ and $q_a(120°) \cong 0.06$ to 0.12 according to Figure 1, the maximum values $\cos \theta_v L_p \cong 0.0175$ correspond to a $\delta_a \cong 0.35$ to 0.70. In picture B, minimum values ranging from $\cos \theta_v L_p \cong 0.002$ to 0.006 are consistent with previous ground-based measurements of vegetation and bare soil polarizations [*Vanderbilt et al.*, 1990; *Rondeaux and Herman*, 1991; *Bréon et al.*, 1995], and show that land surface polarization is generally no larger than aerosol polarization. Moreover, the smoothness of the minimum picture confirms that land surface polarization exhibits lower spatial variability than land surface reflectance, hence making the correction of the measurements easier.

On the other hand, comparison of pictures A and B shows that very clear conditions probably never prevail over polluted areas like China or the Ganga basin, therefore preventing the estimation of the surface polarization by a simple minimum technique. The applicability of the method clearly needs some general modeling of the land surface BPDF according to the land surface geotype, as achieved by *Nadal and Bréon* [1999].

Another qualitative example is provided by (Plate 1, bottom) composites of POLDER pictures acquired over occidental South Africa on June 4 and 23, 1997, at the very beginning and at the height of the biomass burning activity, respectively, as confirmed by the ATSR-2 fire products [*Goloub and Arino*, 2000].

The viewing direction selected for each pixel corresponds again to a constant scattering angle (here $\Theta = 110°$). Moreover, the two orbits differ from a few POLDER subcycles (about 4 days), so the viewing geometries and thus the surface contribution should be nearly the same in the two pictures. For each day, images B and P display in true color the radiances and polarized radiances measured in the three channels. Because of the importance of the molecular polarization at 443 nm, the molecular contribution has been subtracted from the polarization data. Clearly, from June 4 to 23, the large increase of the extended plume of biomass burning aerosols is more discernible in the polarized radiance picture than in the radiance one. Note that the yellow color of the polarized picture is quite a persistent feature, which shows that most aerosols scatter less polarized light at short wavelengths.

3.2. Level 2 Aerosol Products

Let us first illustrate the algorithm functioning on typical measurements. Figure 5 shows the case of a pixel in the Ganga valley, near New Delhi. Rather than level 1 data (Q_0, U_0), Figure 5 displays the polarization angle and polarized radiance (ψ, L_p) as a function of the scattering angle. Figure 5a confirms that the polarization direction, as expected, is nearly orthogonal to the scattering plane except in backscattering directions where the polarized light becomes very small. In these directions the aerosol single-scattering contribution vanishes and multiple-scattering processes result in more involved polarization behavior. In the present case, the aerosols exhibit probably negative polarization (parallel to the scattering plane) in a small angular range near $\Theta = 170°$, but analysis of such effects is out the scope of our simplified modeling. Figures 5b and 5c show the polarized radiances. Different labels indicate the raw measurements ($L_p^{\text{meas}} = \sqrt{Q_0^2 + U_0^2}$), the molecular contribution ($L_p^m = Q_m$), the measurements corrected from the molecular effect ($(L_p^{\text{meas}} - L_p^m)e^{\delta_m M}$), the surface contribution (L_p^g), and the retrieved signal ($|Q_{\text{cal}}|$), respectively. The retrieved optical thickness here is $\delta_0 = 0.44$, with $\alpha = 1.38$. Over this highly polluted pixel the aerosol contribution is well above the molecular and ground contributions, and the inversion scheme allows a correct fit of the measurements.

Examples of global results derived in this way are shown in Plate 2 as maps of the retrieved aerosol optical thickness (pictures iA and MA) and Ångström exponent (pictures iB and MB). Pictures iA to iC (Plate 3) are for measurements over the whole Indian subcontinent on November 14, 1996 (two consecutive orbits), and pictures MA to MC are for measurements over Mexico on May 27, 1997. For comparison, the results

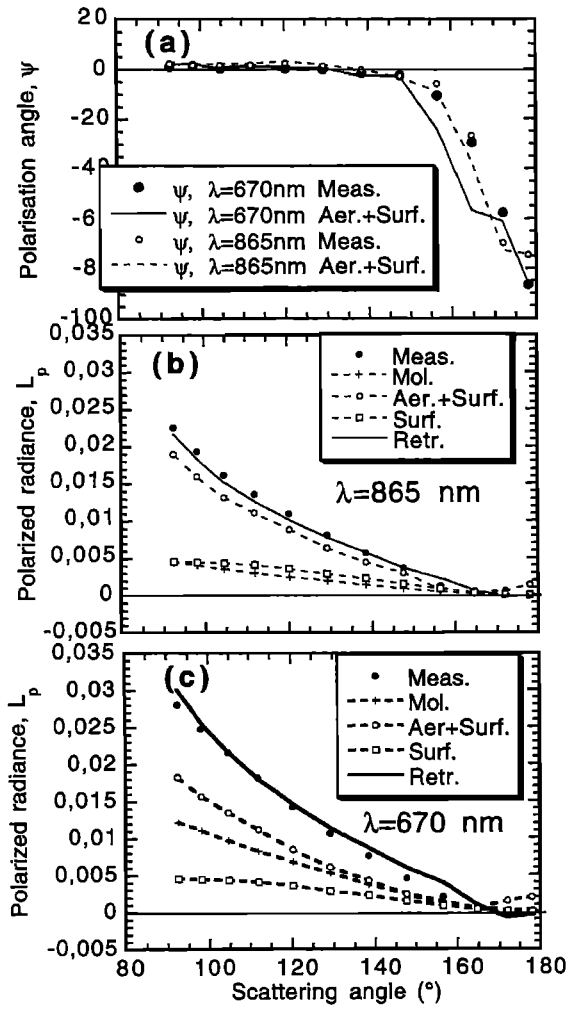

Figure 5. POLDER observations over a pixel in the Ganga basin, near New Delhi. (a) Measurements and calculations of the angle between the polarization direction and the perpendicular to the scattering plane, ψ, as a function of the scattering angle corresponding to the viewing direction. Solid circles and open circles: measurements at 670 and 865 nm, respectively. Solid and dashed curves: calculations at 670 and 865 nm, respectively. The polarized vibration is perpendicular to the scattering plane, except in backward directions where multiple scattering and/or changes in the aerosol polarization direction make the polarization behavior more complex. (b) As Figure 5a but for polarized light at wavelength λ = 865 nm. Measurements (solid circles) compare well with calculations for the retrieved aerosol model (solid line). The surface and molecular contributions are indicated. (c) As Figure 5b but for wavelength λ = 670 nm.

obtained over the ocean in a very different way [*Deuzé et al.*, 1999] are reported also. As these last results are derived from more confident radiance data and compare well with correlative ground-based measurements [*Goloub et al.*, 1999], comparison allows an indirect validation of the land products.

The global distribution of the aerosol optical thickness over land is not unrealistic. In pictures iA to iC (Plate 3), for example, the known pollution prevailing within the Ganga basin contrasts with lower loading over the main Indian continent, and the orders of magnitude of δ_0 and α are reasonable. In pictures MA to MC the large aerosol loading of small particles with large Ångström exponents is consistent with biomass burning activity in this region in May. However, while the results obtained over land and over the ocean are rather consistent in pictures MA to MC, they differ markedly in pictures iA to iC. Such a discrepancy between the results of the two processing lines over coastlines is a common feature of similar comparisons. The exception is when the results over the ocean indicate very small particles with a high Ångström exponent. Generally, the inversion scheme over land underestimates the optical thickness, while it overestimates the Ångström exponent, which suggests some systematic bias in the aerosol products over lands.

4. Comparison With Ground-Based Measurements

The reliability of the results has been assessed more directly from comparison with direct measurements of δ_0 and α achieved by ground-based Sun photometers. Data obtained during the POLDER overpass, with clear-sky conditions according to the POLDER cloud mask, have been selected in the data bank of AERONET (Aerosol Robotic Network) [*Holben et al.*, 1998] or provided independently by T. Nakajima, R. Santer, and V. Soufflet. Table 1 lists the stations where these correlative measurements were performed. Note that a lot of the data concerns desertic sites.

The methodology of the comparison is explained by *Goloub et al.* [1999]. Filtering of the Sun photometer data was performed in order to select measurements (1) simultaneous to the satellite overpass within half an hour, (2) corresponding to stable atmospheric conditions, (3) specially controlled to prevent undetected subpixel clouds, and (4) with a large enough aerosol content; only observations with $\delta_0 > 0.05$ were retained. The POLDER results are averaged over a 100 × 100 km^2 area around the ground station (average of 5 × 5 boxes of 3 × 3 pixels each).

The comparison between the POLDER and the Sun photometer results is shown in Figures 6a and 6b, respectively, for α and δ_0. Both results are extremely noisy, as seen also in Plate 2 when comparing the very different qualities of the products over the land and over the ocean. This is not too surprising. The uncertainty on the surface contribution, typically $\Delta L_p^g \cong 0.001$ to 0.002 according to *Nadal and Bréon* [1999] is noticeable compared with the aerosol contribution, generally about $L_p^a \cong 0.010$. However, the outstanding feature in Figures 6a and 6b is the systematic bias in the α and δ_0 retrievals, which confirms the previous results over coastlines. In most cases the retrieved Ångström exponent is overestimated, while correlatively, the aerosol optical thickness is underestimated. For all measurements, Figure 6c shows how the optical thickness ratio $\delta_0^{\text{POLDER}}/\delta_0^{\text{SUNPH.}}$ varies as a function of α. The linear fit is indicated. The aerosol optical thickness derived from POLDER is largely underestimated for large aerosols and tends progressively toward consistent figures for very small aerosols, as outlined previously.

5. Discussion: Aerosol Index

5.1. Biases of Results and Bimodality of Aerosols

Let us focus on the polarized light scattered in side-scattering directions, in the range 80° < Θ < 120° where polarization is large (see Figure 5). Polarization features like the rainbow should deserve a specific study. In side-scattering

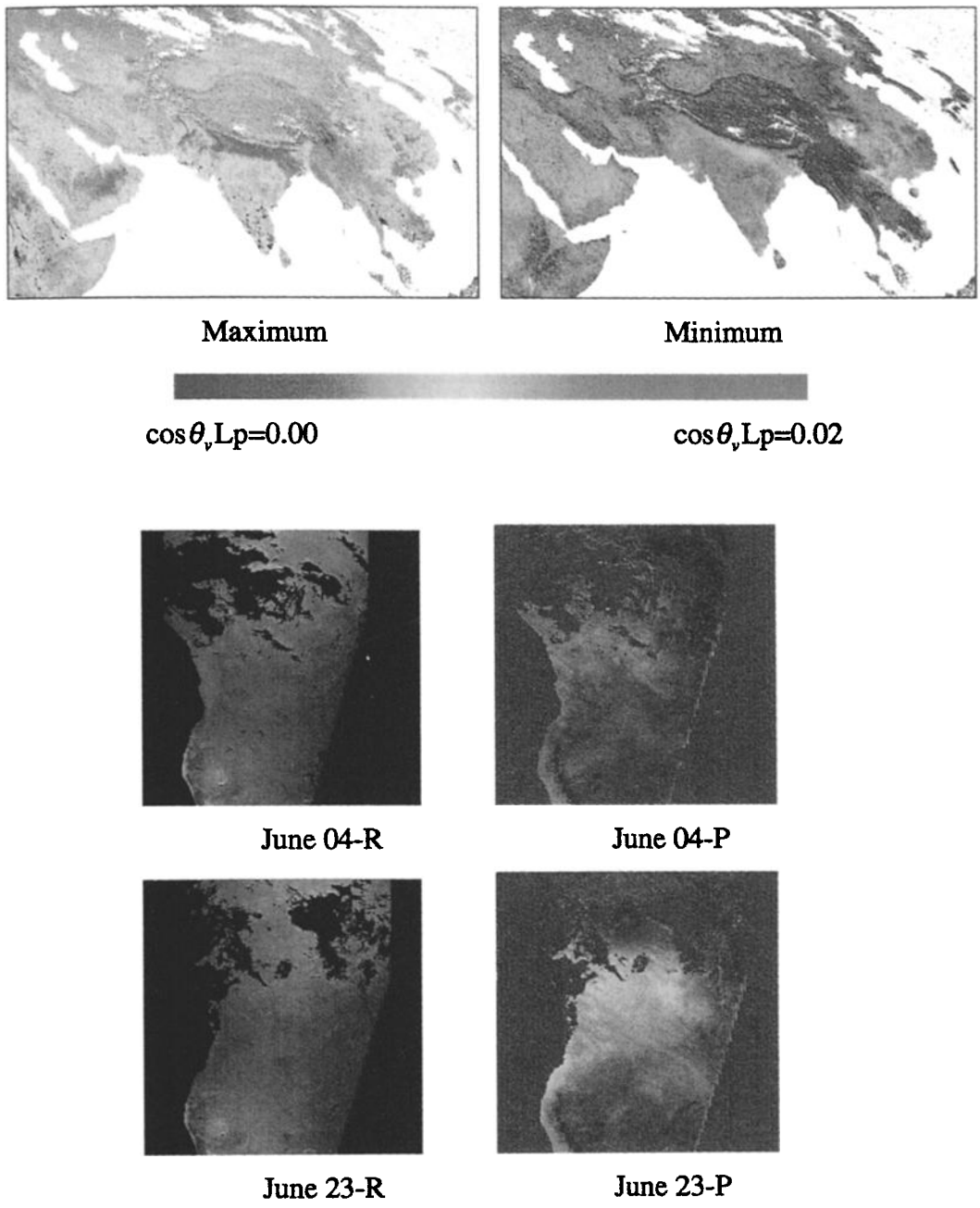

Plate 1. (top) (maximum and minimum): For each ground pixel of the area, the images display the maximum and minimum value, respectively, of cos $\theta_v L_p$ observed over a 1 month period with cloudless conditions. To minimize variations in surface reflection and aerosol-polarized phase function, the data correspond to a viewing direction providing a constant scattering angle (Θ = 120°). Qualitatively, the images are expected to display the land surface and the largest aerosol contributions in polarized light. Minimum image confirms that the land surface contribution does not exhibit large spatial variability, and comparison with maximum image shows that the aerosol contribution may be well above the surface contribution. (bottom) True color composites (443 nm, blue; 670 nm, green; 865 nm, red) of POLDER pictures over occidental South Africa, on June 4, 1997 and June 23, 1997, for radiance (R) and polarized radiance (P); polarized radiances are corrected for molecular scattering. The large plume of biomass burning aerosols, which appears on June 23, is more discernible in polarized light.

directions it is well known that the polarizing efficiency of scattering increases when the particle dimension decreases [*Hansen and Travis*, 1974], so polarization measurements allow detection of only the smaller particles within the aerosol size distribution. Therefore the bias in the optical thickness retrieval indicates that the implicit relationship between large/nonpolarizing and small/polarizing particles entailed by our aerosol modeling is wrong. Two simple possibilities can be examined in a first approach. An obvious explanation is that some particles, because they are nonspherical, provide less

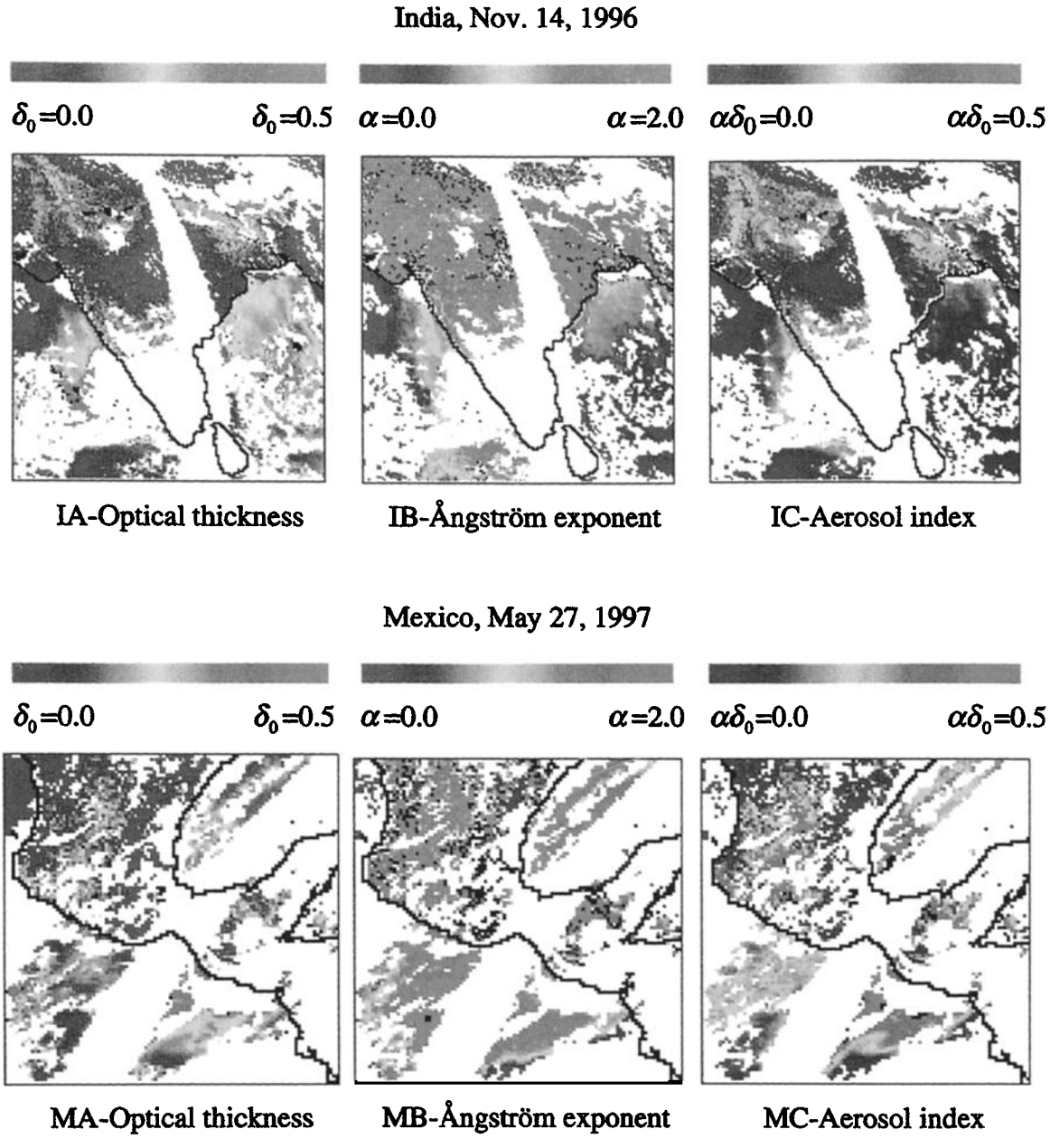

Plate 2. (top) (IA to IC): Aerosol parameters derived from POLDER. Comparison between the results over land derived from polarized light (present paper), with the more confident results over ocean derived mainly from total light [*Deuzé et al.*, 2000]. The observed area is over India; POLDER orbits 3161 and 3162, on November 14, 1996. For each cloud-free pixel, image iA displays the retrieved optical thickness δ_0, image iB, the retrieved Ångström exponent α, and image iC, the product $\delta_0\alpha$. The color codes are indicated, increasing values from blue to red. For these urban-industrial aerosols the results over land and over ocean contrast over coastlines, indicating overestimation of α and underestimation of δ_0 over land. Image iC indicates compensation of the biases in the aerosol index $AI = \delta_0\alpha$. (bottom) (MA to MC): Same legend but for an area over Mexico; POLDER orbits 8012 and 8013 on May 27, 1997. For these small biomass burning aerosols the results are reasonably consistent on either sides of the coastlines, indicating that POLDER results over land are consistent.

polarized light than expected according to Mie theory, which should explain the underestimation of the optical thickness. Another simple possibility is that by assuming monomodal size distribution we underestimate the number of large/nonpolarizing particles linked to the small/polarizing ones. This defect may appear for pronounced bimodality of the size distribution, and ground-based observations have shown that many aerosols exhibit significant bimodality [*Shettle and Fenn*, 1979; *Nakajima et al.*, 1996; *Remer and Kaufman*, 1998].

Let us consider the POLDER observations over the ocean, which provide both the total and the polarized light scattered by the aerosols. As explained by *Deuzé et al.* [2000], these observations are also analyzed with monomodal aerosol models but the inversion starts with the total radiance in the 670

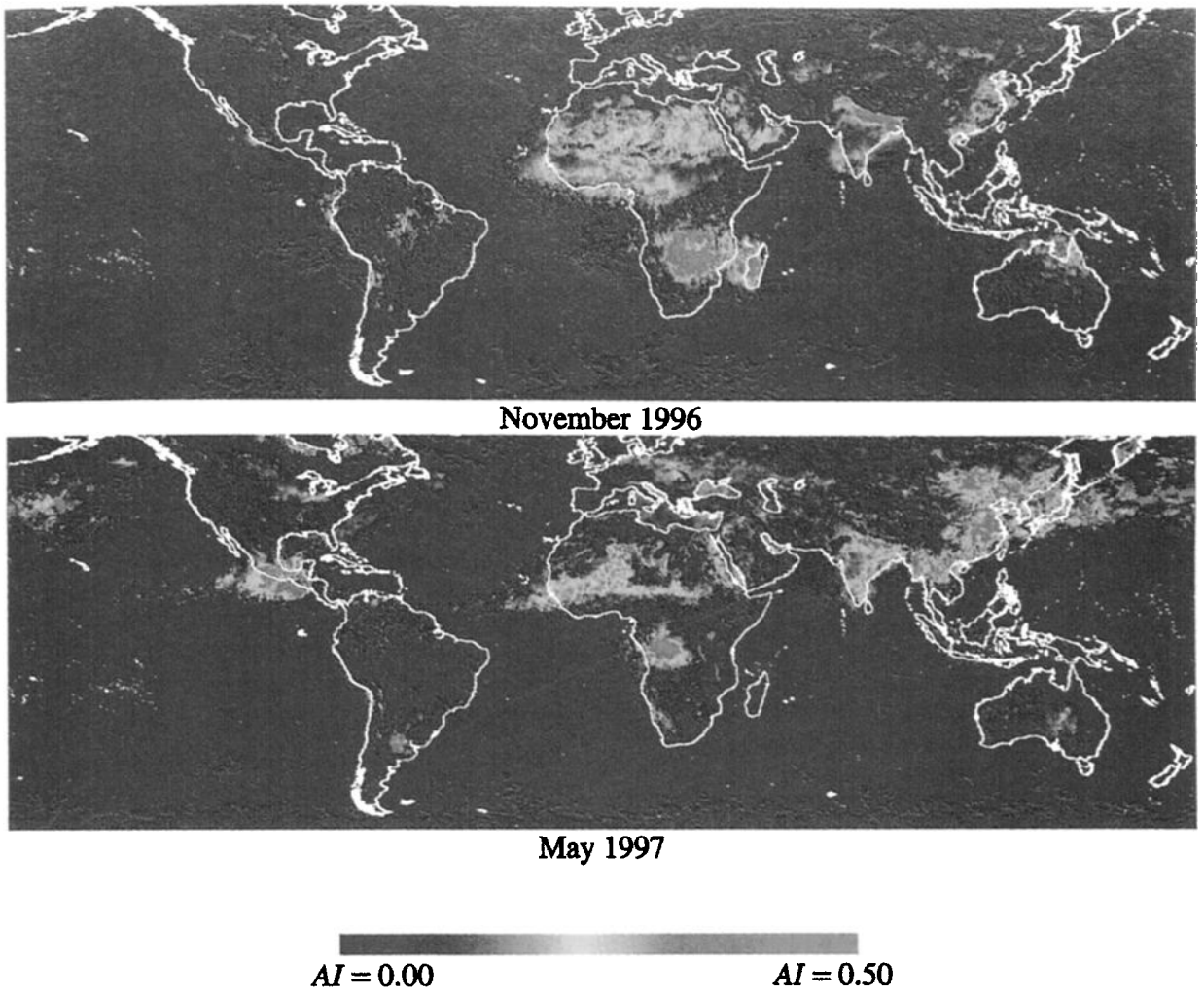

Plate 3. One month average values of the aerosol index $AI = \delta_0\alpha$. (top) November 1996, (bottom) May 1997. While the POLDER aerosol-processing lines over land and ocean lead to δ_0 and α results, which may differ largely though coastlines, the aerosol index exhibits good continuity and allows for detecting large pollution sources (Indian continent, China), areas of biomass burning activity (Madagascar and South Africa in November, Mexico in May), and Saharan aerosols.

and 865 nm channels. These theoretical monomodal models enable a fit of the radiance and lead to values of δ_0 and α consistent with ground-based observations [*Goloub et al.*, 1999], but they tend to underestimate the polarized light measured in side-scattering directions [*Deuzé et al.*, 2000]. This trend is inconsistent with the hypothesis of nonpolarizing particles but is very understandable in the presence of bimodal size distribution of the aerosols. Let us consider according to *Remer and Kaufman* [1998] a size distribution consisting of a small accumulation mode and a large coarse mode. Mie calculations show that the coarse mode gives negligible polarized light in the range $80° < \Theta < 120°$, while its contribution in the total light is noticeable. Then, as shown qualitatively in Figure 7a and confirmed by numerical simulations [*Deuzé et al.*, 2000], because the monomodal model has to take into account the contribution of the coarse mode in the total radiance, its adjustment is at the expense of the small particles, which leads to underestimation of the polarized light. Conversely, it can be seen that in the present algorithm, where the monomodal model only accounts for polarized light, it adjusts on the accumulation mode as shown qualitatively in Fig. 7b, at the expense of the large particles and their contribution in δ_0 and α, thus leading to larger α and smaller δ_0.

Table 1. List of the Stations Where Correlative Aerosol Measurements Used for POLDER Validation Have Been Performed, With Number of Observations Available According to Different Filterings

	Site Name	Location	Number of Filtered Data
Europe/France	Aire/Adour	43.7°N, 0.2°E	24
Europe/France	Lille	50.5°N, 3°E	5
Europe/France	Wimereux	50.7°N, 1.6°E	30
Asia/Japan	Niigata	38°N, 139°E	21
Africa/Senegal	Dakar	14.4°N, 16.9°W	40
Africa/Burkina Fasso	Bidibahn	14°N, 0.5°W	27
Africa/Burkina Fasso	Bondoukoui	11.8°N, 3.75°W	39
Africa/Niger	Banizoumbou	3.5°N, 2.6°E	57

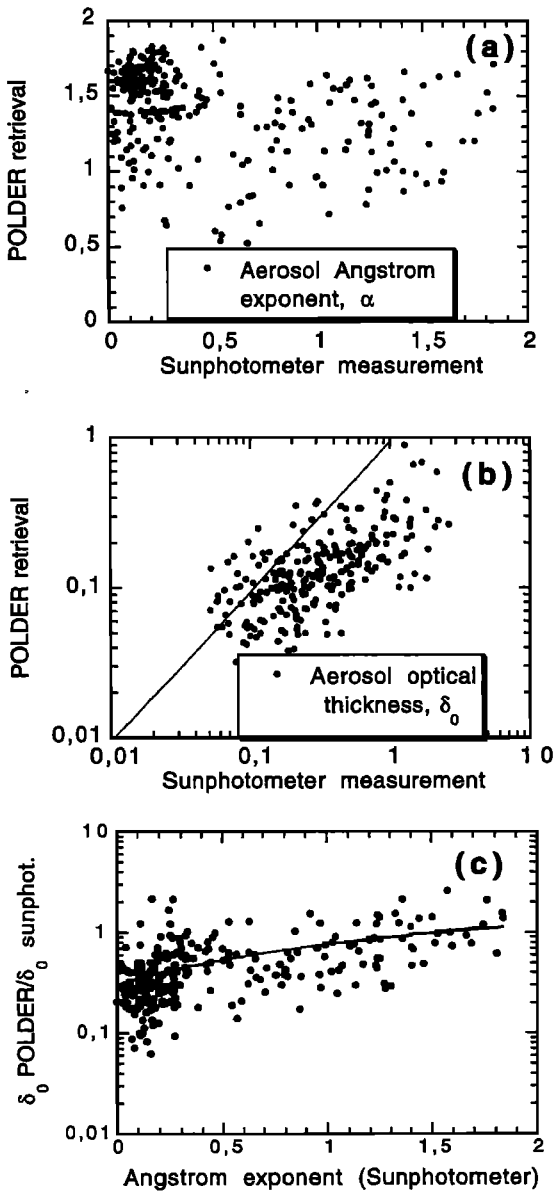

Figure 6. (a) Comparison of the aerosol Ångström exponent derived from POLDER with that derived from Sun photometer measurements. Polarized light systematically leads to an overestimation of α. (b) As Figure 6a, but for the aerosol optical thickness at 865 nm. Polarized light systematically leads to an underestimation of δ_0. (c) The ratio $\delta_0^{\text{Polder}}/\delta_0^{\text{Sun-Phot}}$ of the aerosol optical thicknesses derived from POLDER and Sun photometers is reported as a function of the Ångström exponent of the particles. The solid line corresponds to linear regression. The POLDER results tend toward consistent values for small particles with a large Ångström exponent.

5.2. Aerosol Index

The discussion suggests that δ_0 and α derived from polarization are characteristics of the small mode of aerosols and correspond to the aerosol global properties only when the size distribution reduces to this mode. A more precise assessment of the physical significance of δ_0 and α requires further analysis of the POLDER data, but the previous analysis may be supported indirectly by examination of the reduced parameter

$$AI = \alpha\delta_0, \tag{11}$$

which, moreover, could provide a convenient aerosol indicator.

Let (α_A, δ_A) and (α_C, δ_C) represent the parameters of the accumulation and coarse modes of a bimodal model, respectively. According to the previous considerations, let us assume crudely that the coarse mode corresponds to $\alpha_C \approx 0$ and gives negligible polarized light, so our inversion leads to (α_A, δ_A). As the Ångström exponents are derived from nearby channels λ_0 and λ_1, with $\delta_{\lambda_1} \approx \delta_{\lambda_0}(1 + \alpha\Delta\lambda/\bar{\lambda})$, the Ångström exponent of the bimodal model is approximately

$$\alpha = \frac{\delta_A\alpha_A + \delta_C\alpha_C}{\delta_A + \delta_C} = \frac{\delta_A\alpha_A + \delta_C\alpha_C}{\delta}, \tag{12}$$

so with $\alpha_C = 0$,

$$AI = \delta\alpha = \delta_A\alpha_A. \tag{13}$$

As shown in the Appendix, the previous crude derivation may be supported by a more refined analysis. Therefore (13) suggests that simple comparison of AI values based on the true aerosol parameters with AI estimates derived only from polarization measurements allows us to check the "bimodal" explanation of the observed biases in δ_0 and α. If this explanation is correct, the aerosol index AI should provide partial characterization of the whole aerosol size distribution from data related only to the small polarizing particles.

5.3. Validation-Aerosol Survey Over Lands and Ocean

The δ_0 and α parameters reported in Figures 6a and 6b have been combined according to (11) in order to compare aerosol indices derived from direct Sun photometer measurements with those derived from the correlative POLDER data. Figure 8 shows that the results are reasonably consistent and that the systematic biases in δ_0 and α are reduced in the resulting AI.

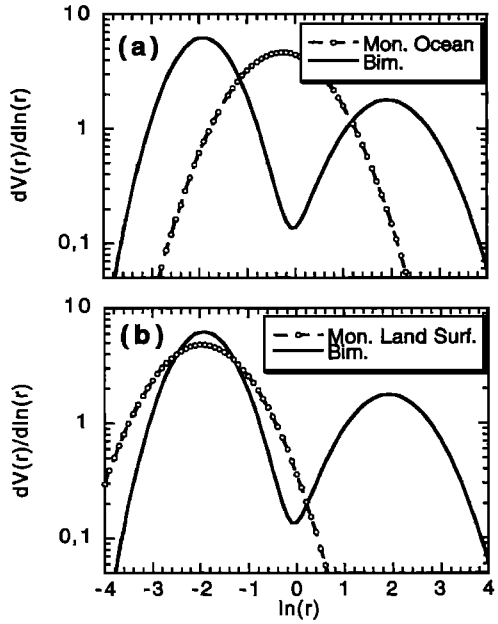

Figure 7. (a) To fit the radiance from bimodal aerosols, the monomodal model of the ocean processing line has to take into account the coarse mode of aerosols, at the expense of a lot of small polarizing particles. (b) Inversely, to fit the polarized radiance, the monomodal model of the land surface processing line has mainly to take into account the accumulation mode of particles, at the expense of the large particles.

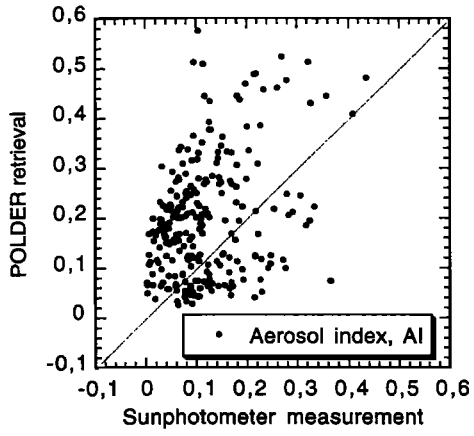

Figure 8. Comparison of the aerosol index AI derived from POLDER with that derived from Sun photometer measurements. The biases in δ_0 and α derived from POLDER (see Figures 6a and 6b) are reduced in $AI = \alpha\delta_0$.

The same transformation has been applied to the aerosol parameters δ_0 and α reported in images iA, iB and MA, MB of Plate 2, and the resulting aerosol indices are reported in images iC and MC of the plate. The systematic discrepancies between the POLDER aerosol results of the two independent processing lines disappear largely when expressed in terms of aerosol index.

Therefore these comparisons support the possibility of combining the present POLDER aerosol results over land in a single aerosol indicator, AI, which despite a reduction in the information about the particles, is related to the entire aerosol distribution.

It is worthwhile to examine the behavior of AI for the particular case of desertic particles. These aerosols are known to consist partly of nonspherical and slightly polarizing particles, so the ability of polarization measurements to detect this important component is questionable. The results of Figure 8 have been dispatched in Figures 9a and 10a according to the Ångström exponent of the particles. Figures 9a and 10a correspond, respectively, to $\alpha > 0.50$ and $\alpha < 0.50$ according to the ground-based values as shown by the histograms of the Ångström exponent in Figures 9b and 10b. Most values of $\alpha < 0.50$ correspond to the three African stations of AERONET and are most likely associated with large dust events.

Strikingly, Figure 10a shows that the aerosol index is sensitive to desertic particles, with a large number of events exhibiting significant values of AI, larger than 0.05 to 0.10. Despite the systematic bias in Figure 10a between the POLDER and the Sun photometer results, which may be indicative of the inadequacy of Mie theory for such particles, the aerosol index derived from polarized light allows qualitative detection of desertic particles.

Finally, Plate 3 shows global maps of the aerosol index derived from the two aerosol-processing lines, over land and ocean, respectively. The results are average values of AI over one month, for November 1996 and May 1997. The consistency between the two kinds of results is impressive. More extensive and in depth analysis of these results should be developed in another paper, but Plate 3 shows that AI detects some large and well-known aerosol sources over land such as the Indian

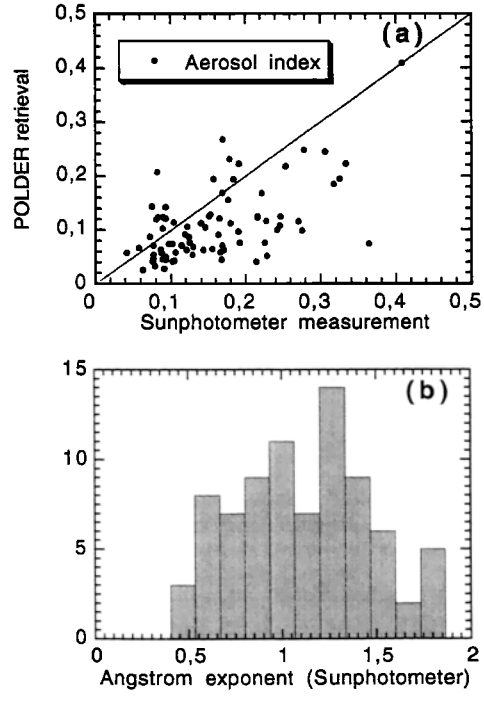

Figure 9. (a) As Figure 8, but the comparison between the POLDER and the Sun photometer AI is shown for the case of rather small particles; $\alpha > 0.50$ according to the ground-based values. (b) Histogram of the Ångström exponent (from ground-based measurements) for observations reported in Figure 9a.

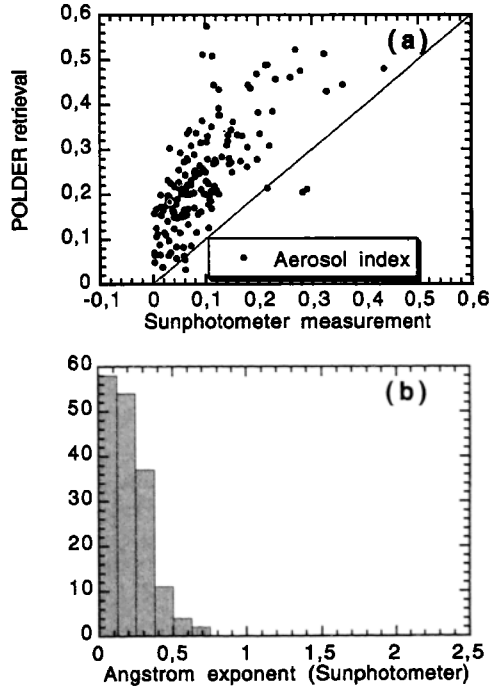

Figure 10. (a) As Figure 8, but the comparison between the POLDER and the Sun photometer AI is shown for the case of large particles; $\alpha < 0.50$ according to the ground-based values. Most results are from AERONET stations in Africa and correspond to Saharan dusts. (b) Histogram of the Ångström exponent (from ground-based measurements) for observations reported in Figure 10a.

continent, the Sahara desert, and China. Major areas of biomass burning activity are particularly well detected, over Madagascar and South Africa in November and over Mexico and China in May. A dedicated analysis of these specific aerosols [*Goloub and Arino*, 2000] highlights a good correlation between the time series of AI with fire occurrences derived from the ATSR infrared channels. Moreover, the main geographical and seasonal aerosol features derived from the POLDER data over the oceans are consistent with the properties of the aerosols derived previously from the NOAA/AVHRR data with respect to their mean content by *Stowe et al.* [1992] and *Husar et al.* [1997] and to their size by *Higurashi and Nakajima* [1999] [*Deuzé et al.*, 1999]. Although resulting in a reduction in information about the aerosols, AI appears as a powerful key in order to achieve a unified global survey of aerosols over both land and ocean.

6. Conclusion

Remote sensing of aerosols over land surfaces is examined by using the polarized light measured by POLDER at near-infrared wavelengths, after due correction for the surface contribution. The polarized light scattered by the aerosols is analyzed through monomodal models of spherical nonabsorbing particles in order to derive their Ångström exponent α and optical thickness δ_0.

Comparisons with in situ measurements show that the retrieved parameters are meaningful for small aerosols, specially biomass burning aerosols, but otherwise are generally biased, with systematic overestimation of α and correlative underestimation of δ_0. Since polarized light is mainly sensitive to scattering by small particles, the biases are probably linked to bimodality of the aerosol size distribution, with the retrieved parameters related to the smaller accumulation mode of particles. POLDER measurements over the ocean, which allow for more in-depth analysis, will be processed with a bimodal inversion scheme. Further examination of these improved results near coastlines should allow a more precise assessment of the significance of the individual parameters α and δ_0 retrieved over land. In a first approach, an aerosol index $AI = \alpha\delta_0$ is proposed. It permits a link between the POLDER aerosol surveys over land and ocean, so the global maps of AI allow some monitoring of the main aerosol sources over continental areas, including desertic particles.

Appendix A

Equation (13) may be supported by a more refined analysis. In order to estimate more precisely how the present algorithm performs with bimodal aerosols, we have computed the Ångström exponents α and polarized phase functions $q_a(\lambda, \Theta)$ for various monomodal and bimodal size distributions. Given the lack of directional information (see Figure 3), we have just calculated $q_a(\lambda, 100°)$ for the fixed scattering angle $\Theta = 100°$.

As the algorithm operates mainly with the ratio of polarized light,

$$X = \frac{L_p^a(\lambda_1)}{L_p^a(\lambda_0)} = \frac{\delta_a(\lambda_1) q_a(\lambda_1)}{\delta_a(\lambda_0) q_a(\lambda_0)},$$

Figure A1 firstly displays the relationship between X and α for monomodal and bimodal models, respectively. According to Figure A1a by fitting with a monomodal model, the X ratio

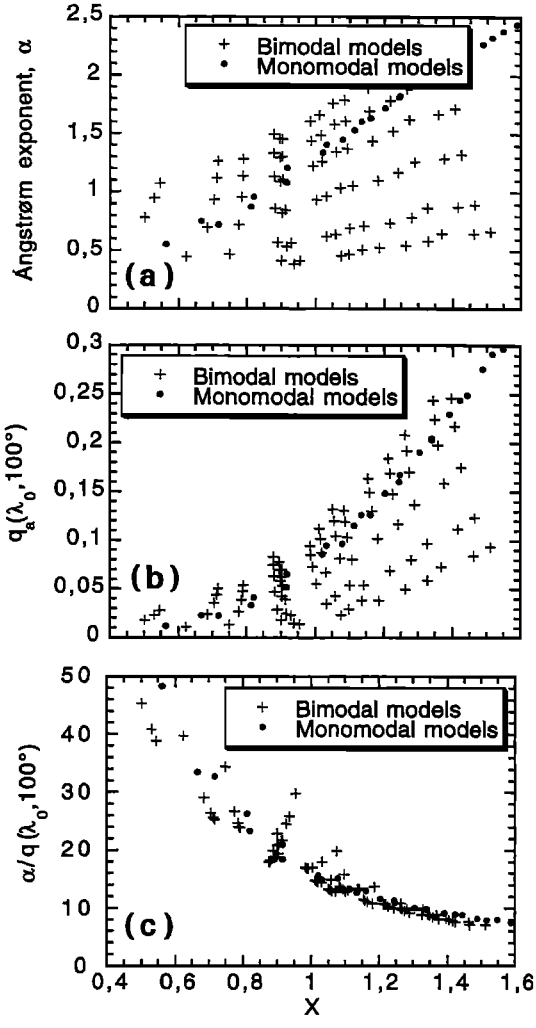

Figure A1. For monomodal and bimodal aerosol models, calculated relationships between the ratio of polarized light X and, respectively (A1a) the Ångström exponent α; (A1b) the polarized phase function $q_a(\lambda_0, 100°)$; and (A1c) the ratio $\alpha/q_a(\lambda_0, 100°)$ of the corresponding model. Given $L_p^a(\lambda_0)$ and $X = L_p^a(\lambda_1)/L_p^a\lambda_0)$ corresponding to bimodal aerosols, estimations based on monomodal models are shown to lead generally to an overestimation of α (Figure A1a), underestimation of δ_0, with $\delta \approx L_p^a(\lambda_0)/q_a(\lambda_0))$ (Figure A1b), but reasonable values of AI with $AI = \alpha\delta_0 \approx (\alpha/q(\lambda_0))L_p^a(\lambda_0))$ (Figure A1c). Monomodal models: lognormal size distribution with $\bar{r}$ varied and σ fixed ($\sigma = 0.8735$). Bimodal models [adapted from *Tanré et al.*, 1997]: two lognormal size distributions with the percentages of the two modes varied; mode 1: $\bar{r}$ varied ($\bar{r}_1 = 0.050$, (0.015), 0, 11 μm) and σ fixed ($\sigma_1 = 0.6$); mode 2: $\bar{r}$ and σ fixed ($\bar{r}_2 = 1.0$ μm, $\sigma_2 = 0.8$). For the two kinds of models: spherical nonabsorbing particles, with refractive index $m = 1.33$, 1.40, and 1.50.

corresponding to bimodal aerosols will generally lead to an overestimation of the Ångström exponent, which is the general trend of the present algorithm. Secondly, Figure A1b compares the relationship between X and $q_a(\lambda_0, 100°)$ for the two kinds of models. Figure A1b shows that $q_a(\lambda_0, 100°)$ is generally smaller for bimodal than for monomodal models. Thus given the polarized light $L_p^a(\lambda_0)$ scattered by bimodal aerosols, the optical thickness $\delta_0 \approx L_p^a(\lambda_0)/q_a(\lambda_0)$ will be underestimated when assuming monomodal models. Finally, as $AI = \alpha\delta_0 \approx$

$(\alpha/q_a(\lambda_0))L_p^a(\lambda_0)$, Figure A1c displays the direct relationships between X and $\alpha/q_a(\lambda_0, 100°)$ for monomodal and bimodal models. Figure A1a confirms that, given X, the biases in α and δ_0 compensate partly in the product $\alpha\delta_0$, so the aerosol index AI derived from the monomodal algorithm will not differ significantly from its true value.

Acknowledgments. Results presented in this paper were obtained using data from CNES's POLDER onboard NASDA's ADEOS. The authors would like to acknowledge A. Lifermann, the POLDER project scientist, for her constant support and helpful comments. The authors are grateful to T. Nakajima of the University of Tokyo, Japan, and to R. Santer and V. Soufflet for the Université du Littoral, France, who kindly provided ground-based measurements. This study was funded by the Centre National d'Etudes Spatiales (CNES), the Centre National de la Recherche Scientifique (CNRS), the Conseil Régional du Nord-Pas de Calais, the Fonds Européen de Développement Régional (FEDER) and the Délégation Régionale à la Recherche et à la Technologie du Nord-Pas de Calais. Informations on POLDER data can be found on the web site http://polder@www-projet.cnes.fr:8060.

References

Bréon, F. M., and S. Colzy, Cloud detection from the spaceborne POLDER instrument and validation against surface synoptic observations, *J. Appl. Meteorol.*, *36*, 777–785, 1999.

Bréon, F. M., D. Tanré, P. Lecomte, and M. Herman, Polarized reflectance of bare soils and vegetation; measurements and models, *IEEE Trans. Geosci. Remote Sens.*, *33*(2), 487–499, 1995.

Bréon, F. M., J. L. Deuzé, D. Tanré, and M. Herman, Validation of spaceborne estimates of aerosol loading from Sun photometer measurements with emphasis on polarization, *J. Geophys. Res.*, *102*, 17,187–17,195, 1997.

Charlson, R. J., S. E. Schwartz, J. M. Hales, R. D. Cess, J. A. Coakley, J. E. Hansen, and D. H. Hofmann, Climate forcing by anthropogenic aerosols, *Science*, *255*, 423–430, 1992.

Deschamps, P. Y., F. M. Bréon, M. Leroy, A. Podaire, A. Bricaud, J. C. Buriez, and G. Seze, The POLDER mission: Instrument characteristics and scientific objectives, *IEEE Trans. Geosci. Remote Sens.*, *32*, 598–615, 1994.

Deuzé, J. L., M. Herman, P. Goloub, D. Tanré, and A. Marchand, Characterization of aerosols over ocean from POLDER-ADEOS-1, *Geophys. Res. Lett.*, *26*, 1421–1425, 1999.

Deuzé, J. L., P. Goloub, M. Herman, A. Marchand, G. Perry, S. Susanna, and D. Tanré, Estimate of the aerosol properties over the ocean with POLDER, *J. Geophys. Res.*, *105*, 15,329–15,346, 2000.

Fraser, R. S., Satellite measurement of mass of Sahara dust in the atmosphere, *Appl. Opt.*, *15*, 2471–2479, 1976.

Goloub, P., J. L. Deuzé, M. Herman, and Y. Fouquart, Analysis of the POLDER polarization measurements performed over cloud covers, *IEEE Trans. Geosci. Remote Sens.*, *32*, 78–88, 1994.

Goloub, P., D. Tanré, J. L. Deuzé, M. Herman, A. Marchand, and F.-M. Bréon, Validation of the first algorithm applied for deriving the aerosol properties over the ocean using the POLDER/ADEOS measurements, *IEEE Trans. Geosci. Remote Sens.*, *37*(3), 1586–1596, 1999.

Goloub, P., and O. Arino, Verification of the consistency of the POLDER aerosol index over land with ATSR-2/ERS-2 fire products, *Geophys. Res. Lett.*, *27*(6), 899–902, 2000.

Gordon, H. R., and M. Wang, Retrieval of water-leaving radiance and aerosol optical thickness over the oceans with SeaWiFS: A preliminary algorithm, *Appl. Opt.*, *33*, 443–452, 1994.

Hagolle, O., A. Guerry, L. Cunin, B. Millet, J. Perbos, J. M. Laherrere, T. Bret-Dibah, and L. Poutier, POLDER level 1 processing algorithms, *SPIE Proc.*, *2758*, 308–319, 1996.

Hagolle, O., P. Goloub, P. Y. Deschamps, H. Cosnefroy, X. Briottet, T. Bailleul, J. M. Nicolas, F. Parol, B. Lafrance, and M. Herman, Results of POLDER in-flight calibration, *IEEE Trans. Geosci. Remote Sens.*, *37*, 1550–1566, 1999.

Hansen, J. E., and A. A. Lacis, Sun and dust versus greenhouse gases: An assessment of their relative roles in global climate change, *Nature*, *346*, 713–719, 1990.

Hansen, J. E., and L. D. Travis, Light scattering in planetary atmospheres, *Space Sci. Rev.*, *16*, 527–610, 1974.

Herman, J. R., P. K. Bhartia, O. Torres, C. Hsu, C. Seftor, and E. Celarier, Global distribution of UV-absorbing aerosols from Nimbus 7/TOMS data, *J. Geophys. Res.*, *102*, 16,911–16,922, 1997.

Herman, M., J. L. Deuzé, C. Devaux, P. Goloub, F. M. Bréon, and D. Tanré, Remote sensing of aerosols over land surfaces, including polarization measurements and application to POLDER measurements, *J. Geophys. Res.*, *102*, 17,039–17,049, 1997.

Higurashi, A., and T. Nakajima, Development of a two channel aerosol retrieval algorithm on global scale using NOAA/AVHRR, *J. Atmos. Sci.*, *56*, 924–941, 1999.

Holben, B. N., et al., AERONET-A federated instrument network and data archive for aerosol characterization, *Remote Sens. Environ.*, *66*, 1–16, 1998.

Husar, R. B., J. M. Prospero, and L. L. Stowe, Characterization of tropospheric aerosols over the oceans with the NOAA advanced very high resolution radiometer optical thickness operational product, *J. Geophys. Res.*, *102*, 16,889–16,909, 1997.

Kahn, R., P. Banerjee, D. McDonald, and D. J. Diner, Sensitivity of multiangle imaging to aerosol optical depth and to pure-particle size distribution and composition over ocean, *J. Geophys. Res.*, *103*, 32,195–32,213, 1998.

Kaufman, Y. J., and J. H. Joseph, Determination of surface albedo and aerosol extinction characteristics from satellite imagery, *J. Geophys. Res.*, *87*, 1287–1299, 1982.

Kaufman, Y. J., and C. Sendra, Algorithm for automatic atmospheric corrections to visible and near-IR satellite imagery, *Int. J. Remote Sens.*, *9*, 1357–1381, 1988.

Kaufman, Y. J., A. Wald, L. A. Remer, B. C. Gao, R. R. Li, and L. Flynn, Remote sensing of aerosol over the continents with the aid of a 2.2 μm channel, *IEEE Trans. Geosci. Remote Sens.*, *36*, 1286–1298, 1997a.

Kaufman, Y. J., D. Tanré, L. A. Remer, E. F. Vermote, A. Chu, and B. N. Holben, Operational remote sensing of tropospheric aerosol over land from EOS-Moderate-Resolution Imaging Spectroradiometer, *J. Geophys. Res.*, *102*, 17,051–17,067, 1997b.

Lafrance, B., Modélisation simplifiée de la lumière polarisée émergeant de l'atmosphère, Correction de l'impact des aérosols stratosphériques sur les mesures de POLDER, thèse de spécialité, Univ. des Sci. et Technol. de Lille, Villeneuve d'Ascq, France, 1997.

Lafrance, B., and M. Herman, Correction of the stratospheric aerosol radiative influence in the POLDER measurements, *IEEE Trans. Geosci. Remote Sens.*, *36*, 1599–1608, 1998.

Legrand, M., M. Desbois, and K. Vovor, Satellite detection of Saharan dust: Optimized imaging during nighttime, *J. Clim.*, *1*, 256–264, 1988.

Martonchik, J. V., Determination of aerosol optical depth and land surface directional reflectance using multiangle imagery, *J. Geophys. Res.*, *102*, 17,015–17,022, 1997.

Nadal, F., and F. M. Bréon, Parameterization of surface polarized reflectance derived from POLDER spaceborne measurements, *IEEE Trans. Geosci. Remote Sens.*, *37*, 1709–1718, 1999.

Nakajima, T., and A. Higurashi, Use of two-channel radiances for an aerosol characterization from space, *Geophys. Res. Lett.*, *25*(29), 3815–3818, 1998.

Nakajima, T., G. Tonna, R. Rao, P. Boi, Y. Kaufman, and B. Holben, Use of sky brightness measurements from ground for remote sensing of particulate polydispersions, *Appl. Opt.*, *36*(15), 2672–2686, 1996.

Nakajima, T., A. Higurashi, K. Aoki, T. Endoh, H. Fukushima, M. Toratani, Y. Mitomi, B. G. Mitchell, and R. Frouin, Early phase analysis of OCTS radiance data for aerosol remote sensing, *IEEE Trans. Geosci. Remote Sens.*, *37*(3), 1575–1585, 1999.

Quenzel, H., and P. Koepke, Tropospheric aerosol optical depth inverted from upwelling radiances, Aerosols and their climatic impact, H. E. Gerber and A. Deepak, (Eds.), pp. 227–240, A. Deepak, Hampton, Va., 1984.

Rao, C. R. N., L. L. Stowe, and E. P. McClain, Remote sensing of aerosols over the oceans using AVHRR data: Theory, practice, and applications, *Int. J. Remote Sens.*, *10*, 743–749, 1989.

Remer, L. A., and Y. J. Kaufman, Dynamic aerosol models: Urban industrial aerosols, *J. Geophys. Res.*, *103*, 13,859–13,871, 1998.

Rondeaux, G., and M. Herman, Polarization of light reflected by crop canopies, *Remote Sens. Environ.*, *38*, 63–75, 1991.

Shettle, E. P., and R. W. Fenn, Models for the aerosols of the lower atmosphere and the effect of humidity variations on their optical properties, *Tech. Rep.*, AFGL-TR-79-0214, Air Force Geophys. Lab., Hanscomb AFB, Mass., 1979.

Stowe, L. L., R. M. Carey, and P. P. Pellegrino, Monitoring the Mt. Pinatubo aerosol layer with NOAA/AVHRR data, *Remote Sens. Environ.*, *60*, 22–34, 1992.

Tanré, D., C. Devaux, M. Herman, R. Santer, and J. Y. Gac, Radiative properties of desert aerosols by optical ground-based measurements at solar wavelengths, *J. Geophys. Res.*, *93*, 14,223–14,231, 1988.

Tanré, D., Y. J. Kaufman, M. Herman, and S. Mattoo, Remote sensing of aerosol properties over the oceans using the MODIS/EOS spectral radiances, *J. Geophys. Res.*, *102*, 16,971–16,988, 1997.

Torres, O., P. K. Bhartia, J. R. Herman, Z. Ahmad, and J. Gleason, Derivation of aerosol properties from satellite measurements of backscattered ultraviolet radiation: Theoretical basis, *J. Geophys. Res.*, *103*, 17,099–17,110, 1998.

Toubbé, B., T. Bailleul, J. L. Deuzé, P. Goloub, O. Hagolle, and M. Herman, In-flight calibration of the POLDER polarized channels using the sun's glitter, *IEEE Trans. Geosci. Remote Sens.*, *37*(1), 513–525, 1999.

Vanderbilt, V. C., L. Grant, and S. L. Ustin, Polarization of light by vegetation, in *Photon-Vegetation Interactions, Applications in Optical Remote Sensing and Plant Ecology*, R. Myneni and J. Ross, (Eds.), Springer-Verlag, New York, 1990.

Vermeulen, A., C. Devaux, and M. Herman, Retrieval of the scattering and microphysical properties of aerosols from ground-based optical measurements including polarization, I, Method, *Appl. Opt.*, *39*(33), 6207–6220, 2000.

Vespérini, M., F. M. Bréon, and D. Tanré, Atmospheric water vapor content from space-borne POLDER measurements, *IEEE Trans. Geosci. Remote Sens.*, 1999.

J. L. Deuzé, C. Devaux, P. Goloub, M. Herman, A. Marchand, G. Perry, and D. Tanré, Laboratoire d'Optique Atmosphérique, Université de Lille 1, 59655 Villeneuve d'Ascq Cedex, France. (jean-luc.deuze@univ-lille1.fr)

F. M. Bréon, F. Maignan, and F. Nadal, Laboratoire des Sciences du Climat et de l'Environnement, Gif sur Yvette, France.

B. Lafrance, Centre National d'Etudes Spatiales, 18 Avenue E. Belin, 31055 Toulouse Cedex, France.

(Received January 11, 2000; revised May 19, 2000; accepted May 28, 2000.)